Evaluation of sea surface roughness parameterization in meso-to-micro scale simulation of the offshore wind field

Xu Ning [*], Mostafa Bakhoday Paskyabi, Hoang Hai Bui, Mohammadreza Mohammadpour Penchah

Geophysical Institute, University of Bergen and Bergen Offshore Wind Centre, Bergen, 5007, Norway

ABSTRACT

Accurate parameterization of the wind-induced effects on the Marine Atmospheric Boundary Layer (MABL) is of fundamental importance for many applications including weather forecasting and offshore wind energy. Roughness parameterizations derived from different datasets are widely used but their performance is not sufficiently assessed under realistic marine environmental conditions. To this end, a multi-scale atmosphere–wave coupled model is constructed for the first time and used in the simulation of the MABL flow over the North Sea. Results show that our model is able to capture the large-scale variation of the mean wind meanwhile reproducing the appropriate turbulence energy cascade in the frequency domain. The performance of different roughness parameterizations is evaluated in comparison with the measurement data from the FINO1 platform. The Taylor-Yelland method outperforms the others on statistics of the mean wind while yielding the highest bias of the Turbulence Kinetic Energy (TKE) from the observations. However, we find that the discrepancy between our simulation and observation mainly depends on the meso-scale model. The magnitude of the differences caused by roughness parameterizations is negligible, especially in low wind speed conditions. The micro-scale simulation is demonstrated as not sensible to the roughness input in the considered wind–wave condition.

1. Introduction

The dynamic system of atmospheric motions involves a wide range of scales in time and space. Numerical models designed for different scales need to use idealized configurations or parameterize the unresolved flow effects in consideration of the limited computational resource (Grooms and Julien, 2018). How to bridge the various scales of the flow and reproduce more realistic atmospheric evolution is thus a challenging problem in many relevant fields such as weather forecasting and wind energy applications. A promising solution is the multi-scale numerical modeling, which utilizes the flow field data obtained from the meso-scale model as the driving force for the micro-scale model with finer temporal and spatial resolutions. Compared with simulations under constant geostrophic wind and stability conditions (Vollmer et al., 2016), the multi-scale simulations driven by the time-varying atmospheric conditions are able to represent the meteorological processes with large-scale variations of wind and temperature

as well as the associated turbulent flow structures (Sanz Rodrigo et al., 2017; Draxl et al., 2021; Bakhoday-Paskyabi et al., 2022a). Moreover, the simulation results can be validated directly by the meteorological measurements and the data from operational wind farms (Liu et al., 2011; Santoni et al., 2020).

Many efforts have been made in previous work to build the model chain nesting meso- and micro-scale simulation codes (Zajaczkowski et al., 2011; Munoz Esparza, 2013; Mirocha et al., 2014) and address the problems in the downscaling process such as the transition in the gray zone (Mazzaro et al., 2017; Haupt et al., 2019; Rai et al., 2019) and the inconsistency of turbulent flows (Muñoz-Esparza et al., 2014; Wu, 2017). The recent studies of boundary layer structure and wind farm flow dynamics showed the superiority of the multi-scale simulations in dealing with atmospheric processes of large spatial and temporal extent, e.g., diurnal cycles (Muñoz-Esparza et al., 2017; Piroozmand et al., 2020) and frontal passages (Arthur et al., 2020;
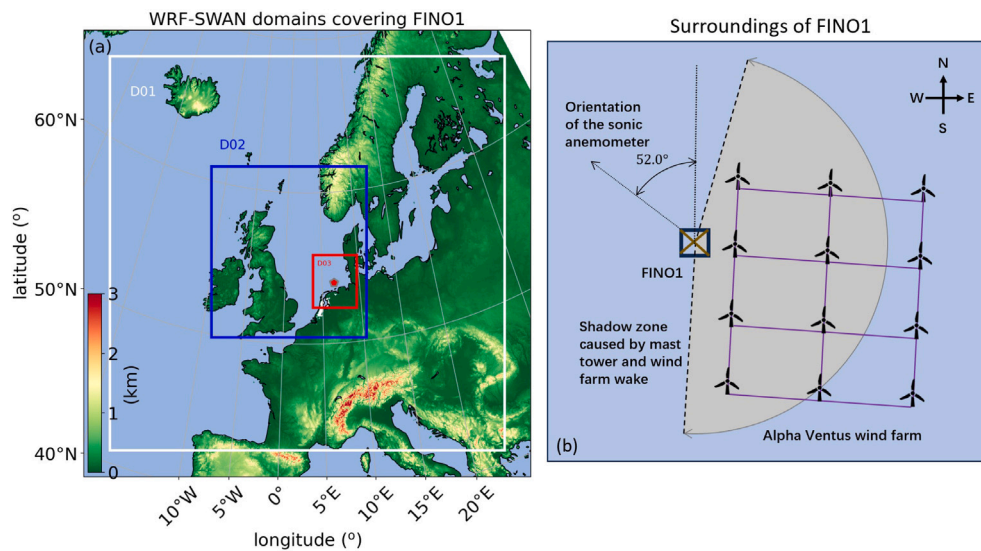
Fig. 1. (a) Topography height and the domains of D01, D02, and D03 used in the WRF simulation. (b) The surroundings of the FINO1 platform.

Bakhoday-Paskyabi et al., 2022b), meanwhile capturing the small-scale turbulence under the effects of surface heterogeneity (Temel et al., 2018; Han et al., 2018; Prósper et al., 2019). However, there are not enough studies that are focused on the multi-scale modeling of the off-shore wind field. The structures and statistics of the offshore wind are directly influenced by the underlying waves. The wave-induced airflow affects the turbulence near the surface and modifies the exchange of momentum and heat between the atmosphere and the ocean (Sullivan and McWilliams, 2010; Wu et al., 2016; Liu et al., 2022). Especially in the case when the swells (non-locally generated waves with relatively high amplitude and propagating speed) play a dominant role, the wave-induced disturbances could reach the height of a wind turbine rotor and significantly affect the performance of wind farms (Kalvig et al., 2014; Yang et al., 2014; AlSam et al., 2015). Therefore, it is a vital problem to represent correctly the wave effects in the multi-scale simulation and more studies are required to advance our knowledge of the features of the MABL under realistic wave regimes.

There are two common methods to consider wave effects in numerical modeling (Deskos et al., 2021). The first one is the wave-phase resolved simulation, which calculates the evolution of the wave field and uses the elevation and the velocity of the wavy surface as the bottom boundary condition for the simulation of the Atmospheric Boundary Layer (ABL) flows above. It is fully based on the governing equations and is able to directly resolve the perturbations in the airflow caused by the moving surface, but the requirement of high resolution in time and space makes it expensive for a multi-scale simulation to cover a long time span and a large domain. This method is usually used in the study of the wind–wave interaction mechanism and wave-induced flow structures within a relatively small domain under idealized conditions (Sullivan et al., 2014; Hao and Shen, 2019). The second uses a fixed mesh with a flat bottom and parameterizes the air–sea fluxes through the modification of surface roughness based on time-averaged wave statistics. In this way, a relatively coarse grid near the surface is acceptable and the wave-induced stress is approximated, saving huge computational costs from handling time-varying surface elevation and wave boundary layer flows. Therefore, wave parameterization is still the preferred choice in multi-scale offshore wind simulation and thus is the method used in the present work. The earliest parameterization of wave effects was proposed by Charnock (Charnock, 1955), who related the aerodynamic roughness length to the surface stress in a proportional law. The fact that this relationship cannot universally describe different datasets leads to the thoughts of subsequent researchers on the possible missed influencing factors. The work of Hsu (1974) and Donelan (1982)

demonstrated the dependency of the Charnock constant on the wave steepness and wave states. Drennan et al. (2003, 2005) tried to find a general formula by fitting it to different field measurements across various conditions but indicated its limited performance in old wave scenarios. Recently, Porchetta et al. (2019) proposed a new roughness parameterization that includes the effects of swell and its misalignment with wind direction using data from measurement campaigns at two different geographical locations.

In the present study, we establish the framework of multi-scale simulation for marine atmospheric boundary layer flows by nesting the meso-scale model WRF-SWAN and the micro-scale LES model PALM. This enables the modeling of offshore wind in realistic sea states and atmospheric stability conditions. The sensitivity of the model to different wave roughness parameterizations is thoroughly investigated in terms of mean wind, turbulence, and spectra in comparison with the observational data. This paper is arranged as following structure. The observational data and the numerical methods are described in Sections 2 and 3 respectively. In Section 4, we present the simulation results and their validation with the measurements, and the discussions and conclusions are summarized in Section 5.

2. Observational data

Observational data were collected from the Forschungsplattformen in Nord- und Ostsee Nr.1 (FINO1), located at 54°0′53.5″N, 6°35′15.5″E, 45 km north of the German coast in the North Sea (Porchetta et al., 2019) (Fig. 1b). The measurements used in this study contain the low-frequency data (10-min averaged) collected from the cup anemometers at 33, 40, 50, 60, 70, 80, 90, 100 m, and the sonic data with 10 Hz sampling frequency at 40, 60 and 80 m heights on the meteorological mast. Additionally, One scanning lidar was specifically adapted to provide vertical wind profiles at the site of FINO1 for 10 min every hour. It should be noted that the sonic anemometers are mounted at the northwest corner of the mast with their primary axes facing a direction of 308° with respect to the North (measured clockwise). This means that wind measurements originating from the area roughly opposite this orientation can be distorted or influenced by the truss structure of the mast itself. Furthermore, the Alpha Ventus wind farm lies just a few hundred meters east of FINO1. The wake flow from the wind farm could also introduce biases to the measurements. A visual representation of the surroundings of FINO1 is provided in Fig. 1. Given the potential contamination from both the mast tower's shadow effect and the wind farm's wake flow, it is necessary to exclude wind data in the range from

Table 1
List of symbols.

Symbol	Dimension	Description
g	m/s^2	Gravitational acceleration
z_0	m	Roughness length
α_c		Charnock parameter
u_*	m/s	Friction velocity
H_s	m	Significant wave height
c_p	m/s	Peak wave phase speed
L_p	m	Peak wave length
Θ	°	Wind direction
Θ_w	°	Wave direction
$\Delta\Theta$	°	Wind–wave misalignment angle
z	m	Height
L	m	Monin–Obukhov length
θ_v	K	Virtual potential temperature
κ		Von Kármán constant
u, v, w	m/s	Velocity components
U_h	m/s	Horizontal velocity
Ri_B		Bulk Richardson number
S_u, S_v, S_w	m^2/s	Spectral density for velocity components

60° to 200.0° to ensure accuracy and reliability in our results. July 6–8, 2015 (referred to as JUL) and September 5–7, 2015 (SEP) were selected for this study. JUL is characterized by a stably stratified boundary layer with moderate winds. A significant feature during this period is the misalignment between wind and wave directions (defined as the direction from which wind or wave comes). SEP, in contrast, features a neutral stability condition where the wind and wave directions align and the wind strength is pronounced. The choice for these periods was driven by the following considerations:

1. Diverse atmospheric conditions and wind–wave regimes: These periods were chosen to encompass a broad range of atmospheric conditions and wind–wave interactions, making our findings more generally applicable. They incorporate both old sea (long-existing waves without significant recent input from local wind) and wind–sea regimes (waves generated by local winds), along with varying degrees of wind–wave misalignment across both neutral and stable atmospheric conditions.

2. Prominent wind–wave interactions: Constrained by the limited computational resources, we prioritized scenarios where the wave effects on the wind would be pronounced so that the four parameterizations might exhibit distinct behaviors. Insights from idealized simulations (elaborated in Section 4.1) indicated that variations in roughness length have more pronounced effects on wind characteristics under conditions of higher wind speeds and stable atmospheric stratification.

3. Dominant wind direction: The primary wind directions during JUL are from the southwest and from the north during SEP. These orientations are the dominant wind directions and are more representative of the area of interest.

4. Data quality: The data of the chosen periods avoids the shadow effects posed by the mast tower and the influence of the wake flow from the wind farm Alpha Ventus located to the east of the measurement platform.

For a comprehensive list of symbols and parameters referenced throughout this paper, please refer to Table 1.

3. Numerical modeling

3.1. Meso-scale simulation

In our study, we used the open-source Weather Research and Forecasting (WRF) Model (ARW version 4.3.1) (Skamarock et al., 2019) for mesoscale atmospheric simulations. We coupled it with the Simulating WAves Nearshore (SWAN) model, a third-generation spectral

wave model (Booij et al., 1997), in a one-way coupling setup. WRF provided 10-meter wind speed data to SWAN, enabling the calculation of essential wave characteristics for determining sea surface roughness length.

The initial and boundary conditions for the WRF are from the hourly ERA5 reanalysis (Hersbach et al., 2020), with the sea surface temperature replaced by the daily OSTIA high-resolution (with a horizontal resolution of roughly 6 km). The SST data from OSTIA are interpolated to hourly inputs to accommodate the ERA5 temporal resolution. For the WRF model, we use three-level nesting domains to cover properly the area of FINO1 and Alpha Ventus offshore wind park with horizontal resolutions of 9 km (D01), 3 km (D02), and 1 km (D03) respectively (shown in Fig. 1a). We use 60 stretched vertical levels with the highest resolution near the surface of about 10 m and 21 levels below the height of 500 m.

The physics parameterization option is chosen from Bui and Bakhoday-Paskyabi (2022) (com2), which uses the Yonsei University scheme (YSU, Hong et al., 2006) for the planetary boundary layer and the Revised MM5 scheme (Jiménez et al., 2012) for the surface layer. Other physics options include the Tiedtke cumulus scheme (D01 only) (Zhang et al., 2011), the Morrison microphysics scheme (Morrison et al., 2009), the RRTM longwave radiation scheme (Mlawer et al., 1997), the Dudhia shortwave radiation scheme (Dudhia, 1989), and the unified Noah land surface model (Mukul Tewari et al., 2004). The Charnock formula was used to calculate the roughness length.

For the SWAN model, two nested domains were defined, corresponding to D02 and D03 in WRF. Bathymetry data was derived from GEBCO bathymetry with a resolution of approximately 400 m. Wave boundary conditions were extracted from the NORA3 hindcast data with a 3-hour temporal resolution. The model utilized 36 frequencies (ranging from 0.05 to 1 Hz) and 36 directional discretizations. Wind input and white-capping, following Janssen (1991), were employed for the source term formulations.

3.2. Meso-to-micro scale nested simulation

Limited by the coarse temporal and spatial resolution, the meso-scale model uses the so-called planetary boundary layer (PBL) scheme (Jia and Zhang, 2020) to parameterize the turbulent mixing effect near the ground. In order to investigate the features of small-scale turbulence in the marine atmospheric boundary layer, the Parallelized Large-Eddy Model (PALM) (Maronga et al., 2020) is offline nested to WRF and SWAN by using their results as boundary conditions. More specifically, the outputs from the innermost domain of WRF including velocity, temperature, and water vapor mixing ratio are provided for the PALM model as the initial 3D flow field and time-varying inflow/outflow conditions at vertical boundaries. The significant wave height, peak wave phase speed, and peak wave direction from the SWAN model are interpolated into the bottom grids of PALM and used in roughness length parameterizations to account for the wave effects. The structure of the model chain is shown in Fig. 2.

3.2.1. LES configuration

Large-eddy simulation cases with different roughness parameterizations are performed under the same meso-scale driving forces from the WRF-SWAN simulation. The one-way online nesting technique is employed in LES cases to represent the wide range of dynamic scales from the meso-scale inflows to the small turbulent eddies in the region of concern. Three domains centered at the geographical location of FINO1 are nested together. The largest one D04 has a domain size of 20.5 km × 20.5 km × 1.9 km with uniform horizontal and vertical grid sizes of 40 m and 20 m respectively. D05 and D06 are its children domains with mesh resolutions in all dimensions twice finer than their parent cases. Domain identifiers and mesh settings for the microscale simulations are summarized in Table 2. A large grid refinement
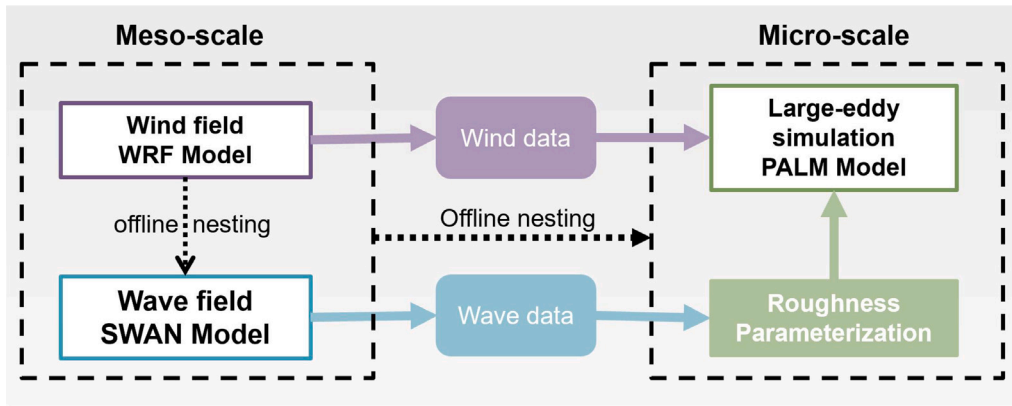
Fig. 2. The model chain of the multi-scale wind–wave coupled simulation.

Table 2
Mesh settings for the micro-scale simulations.

Domain ID	Domain size $L_x \times L_y \times L_z$	Horizontal grid size	Vertical grid size
D04	20.5 km × 20.5 km × 1.9 km	40 m	20 m
D05	10.2 km × 10.2 km × 0.96 km	20 m	10 m
D06	5.1 km × 5.1 km × 0.48 km	10 m	5 m

ratio from D03 (where the meso-scale driving data are collected) to the outermost LES domain D04 is chosen to skip the resolution in the so-called gray zone (Muñoz-Esparza et al., 2017). All LES cases use the third-order Runge–Kutta time advancement and the fifth-order upwind scheme as spatial discretization. The time step is automatically determined online under the Courant–Friedrichs–Lewy (CFL) criterion and the diffusion criterion to maximize computational efficiency and numerical stability. Specifically, the CFL condition requires that the flow does not traverse more than one grid cell per time step, i.e. the CFL number $C = V \Delta t / \Delta L < 1.0$, where V denotes the flow velocity, Δt the time step, and ΔL the grid spacing. We set an upper threshold for C at 0.9, ensuring that, despite fluctuations in actual CFL numbers due to local flow variations, they remained below this upper limit. The turbulent closure for LES is achieved by the 1.5-order SubGrid-Scale (SGS) model according to Deardorff (1980), which calculates the SGS eddy diffusivity of momentum and heat by solving a prognostic equation of SGS turbulence kinetic energy. Since the boundary inputs from WRF are non-turbulent flow, a synthetic turbulence generator is used to accelerate the generation and development of the turbulent eddies and to reduce the width of the transition area in the outer part of the domain (Kadasch et al., 2021).

3.2.2. Roughness parameterization

To estimate the momentum and heat fluxes between the air and ocean, a wall-stress model based on the Monin–Obukhov Similarity Theory (MOST) (Monin, 1954) is employed as the bottom boundary condition. A logarithmic wind speed profile is assumed within the first grid level and the surface fluxes are calculated based on the local air velocity, stability, and aerodynamic roughness length. Therefore, the parameterization of roughness length is crucial to correctly simulate the momentum exchange at the water surface. Unlike in many LES studies of the atmospheric boundary layer over land, where the roughness length is usually prescribed as a fixed value, the ocean surface is neither steady nor homogeneous and should be taken into account. The most commonly used roughness parameterization for the offshore environment is the Charnock model (Charnock, 1955), which assumes that the roughness length is proportional to the friction at the ocean surface,

$$z_0 = \alpha_c \frac{u_*^2}{g}, \tag{1}$$

where z_0 is the roughness length, u_* is the friction speed, g is the gravitational acceleration, and α_c is an empirical constant depending on the sea state called Charnock parameter. However, the Charnock parameter was found to have a large disparity among different field studies (Deskos et al., 2021). To reduce this uncertainty, Charnock's model was improved by Drennan et al. (2003) using wave age scaling,

$$\frac{z_0}{H_s} = 3.35 \left(\frac{u_*}{c_p} \right)^{3.4}, \tag{2}$$

where H_s is the significant wave height, c_p is the peak wave phase speed. Taylor and Yelland (2001) proposed another similar parameterization but used peak wave steepness scaling instead,

$$\frac{z_0}{H_s} = 1200 \left(\frac{H_s}{L_p} \right)^{4.5}, \tag{3}$$

where L_p is the peak wavelength. The performance of these two parameterizations was examined by Drennan et al. (2005) with the datasets obtained under different wind–wave regimes, with the former one better for pure wind–sea states and the latter more suited to mixed sea conditions, but both models were found to perform poorly in swell-dominant sea states. This led to later studies on improving the roughness parameterization in old wave conditions by considering the difference between the mean wind direction and the peak wave propagation direction. Based on Drennen's idea, Porchetta et al. (2019) proposed a new formulation that includes the direction misalignment Θ between wind and wave,

$$\frac{z_0}{H_s} = 20 \cos(0.45\Delta\Theta) \left(\frac{u_*}{c_p} \right)^{3.8 \cos(-0.32\Delta\Theta)}. \tag{4}$$

which gives enhanced roughness length for increasing misalignment.

Under the assumption of a deep-water wave with $H_s = 1.0$ m, Fig. 3 illustrates the variation in roughness lengths determined by the four methods as a function of the friction velocity. The parameterization of Taylor-Yelland only takes the wave steepness effect into account, thereby making it invariant to changes in u_*. Among the remaining methods, Porchetta's formula yields the highest value of z_0 while the lowest is produced by Charnock's equation given the same c_p. Notably, z_0 determined by Eq. (4) exhibits an increase of over an order of magnitude as the wind–wave misalignment angle Θ shifts from 0.0° to 180.0°, a trend particularly pronounced at low surface friction. Despite the fact that there is no universal parameterization that works well in diverse conditions, it is valuable to compare the performance of existing roughness length models in the context of multi-scale simulation and investigate why they are superior or inferior to others in a certain wind–wave condition. To this end, the four roughness parameterizations mentioned above are implemented in our model chain, for which the required wave properties are obtained from the SWAN model.
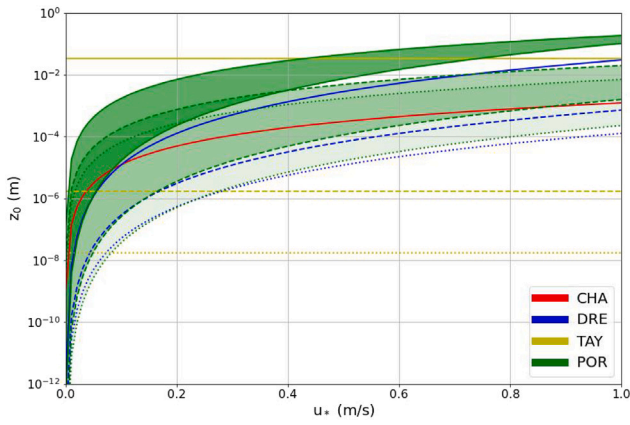
Fig. 3. Variation of roughness length with the friction velocity. Red, blue, yellow and green represent the roughness lengths calculated by Eqs. (1), (2), (3) and (4) respectively. Solid, dashed, and dotted lines are results with $c_p = 4.0, 12.0, 20.0 \, \mathrm{m/s}$. The green region covers the results by Eq. (4) with $0.0 < \Theta < 180.0$.

4. Results

4.1. Idealized simulations

To explore the large-eddy simulation model's sensitivity to roughness length without meso-scale forcing influences, we conducted idealized simulations with roughness length z_0 varying from 1.0×10^{-5} m to 1.0×10^{-2} m. Three geostrophic wind speeds were chosen (3.0 m/s, 5.0 m/s, and 10.0 m/s), alongside three distinct stability conditions (neutral, convective, stable) to encompass a broad range of scenarios. The convective and stable stratifications were achieved by setting a surface heat flux of 0.02 K m/s and a cooling rate of -0.05 K/h, respectively. The vertical profiles for mean wind speed and turbulence kinetic energy (TKE) are illustrated in Figs. 4 and 5 respectively. From the depicted results, we can qualitatively draw the following conclusions:

1. An increased roughness length corresponds to a lower wind speed, stronger wind shear, and more intense turbulence near the surface.
2. Both the geostrophic wind and stability condition determine the strength and vertical reach of the roughness effect.
3. As the geostrophic wind increases and the boundary layer flow is more stably stratified, the influence of roughness length becomes more pronounced, and vice versa.
4. Under stable conditions, the impact of surface roughness penetrates and reshapes the entire boundary layer flow.

4.2. Multiscale simulations

4.2.1. Boundary layer structure and wind–wave regime

The two selected scenarios exhibit distinct stability conditions. This can be quantitatively described using the Monin–Obukhov length, calculated as

$$L = -\frac{u_*^3 \overline{\theta}_v}{\kappa g \overline{w'\theta_v'}}. \tag{5}$$

$\overline{\theta}_v$ is the mean virtual potential temperature, $\overline{w'\theta_v'}$ is the surface virtual potential temperature flux, and κ is the von Kármán constant. The inverse of this length, L^{-1}, acts as an intuitive measure for the static stability of the surface layer. A negative value of L^{-1} indicates a convective condition with upward heat flux. Conversely, a positive value points to a stable boundary layer with downward heat flux. As L^{-1} approaches zero, the flow tends to exhibit neutral stability. In

addition, we calculated the boundary layer height by the criterion of bulk Richardson number Ri_B (Heinze et al., 2017),

$$Ri_B = \left(\frac{g}{\theta_{v,s}}\right) \frac{\Delta\theta_v \Delta z}{(\Delta u)^2 + (\Delta v)^2} \tag{6}$$

where $\theta_{v,s}$ is the virtual potential temperature at the sea surface, $\Delta\theta_v$ is the virtual potential temperature difference across the layer of thickness Δz from the sea surface to the corresponding height, Δu and Δv are the differences of horizontal velocity components across the same layer. The bulk Richardson number quantifies the thermal and frictional forcing by the gradient ratio of temperature and wind speed. The critical value of bulk Richardson number $Ri_{B,c} = 0.25$ is a robust boundary between the dynamically unstable flow ($Ri_B < Ri_{B,c}$, where the flow tends to maintain a turbulent state) and the dynamically stable flow ($Ri_B > Ri_{B,c}$, where turbulence is thermally suppressed). The depth of the boundary layer z_i is thus defined as the height where Ri_B equals $Ri_{B,c}$.

In Fig. 6, the left column provides insights into the atmospheric conditions during the JUL case. Measurements of L^{-1} at a height of 15 m suggest that the airflow exhibited neutrality for the first 18 h, transitioning to a predominantly strong stable condition thereafter. This behavior is reproduced well by the WRF model (see Fig. 6b and c), showing the transition was triggered by the invasion of warm air from the southwest. During the transition, the wind speed at the surface rapidly slowed down and the turbulence was enormously suppressed, with the boundary layer height falling to only tens of meters (white solid line). For the SEP case, a neutral layer was predominantly observed throughout the 2-day span, as indicated by the value of L^{-1} close to 0.0 (Fig. 6d) and the uniformly distributed temperature profile for most of the time (Fig. 6e). The WRF result for this period was also characterized by a remarkably increased wind speed across the boundary layer between 12 h and 32 h.

To further reveal the evolution of the wind–wave regime and the performance of the meso-scale model, the time series of both wind and wave parameters at the FINO1 position from the WRF-SWAN model for JUL and SEP are plotted in the left and right columns of Fig. 7 respectively, compared with the measurement data. The friction velocity reflects the intensity of momentum exchange at the air–sea surface, determining the strength of the local wind-generated waves. The wave age, represented as the ratio c_p/u_*, serves as an indicator of the wind-sea conditions. A c_p/u_* value under 20.0 denotes waves as "young", generated by local winds. Conversely, values exceeding this threshold categorize waves as "old", often referred to as swells (Cohen and Belcher, 1999). Fig. 7a and d illustrate the wind-sea states for JUL and SEP, with periods characterized by older sea conditions highlighted in light blue. During JUL, an older sea state prevailed from 12:00 on July 6 to 19:00 on July 7. This can be attributed to a combination of decreasing wind speeds and the atmospheric transition from a neutral to a stable state, which restrained turbulence at the ocean surface. On the other hand, SEP predominantly experienced young sea conditions, except for the few hours near the end of September 7. The directions of wind and wave can also provide important information on wind–wave interactions. In Fig. 7b and e, the light gray region marks the period when wind–wave misalignment was larger than 60°, and this is only possible in an old sea condition since waves generated by local wind should always follow the mainstream of wind. The meso-scale model captured well the shift of the wind between the west and the south during the second day of the JUL case. For the SEP case, our simulation replicated a consistently northward wind throughout the observed period. The significant wave height showed a strong correlation to the friction velocity as expected. Fig. 7c and f show a close alignment between the model and observed H_s for JUL. For SEP, SWAN followed well the variation trend of H_s as measured but with a consistent bias of about -1.0 m. This discrepancy might arise from an inadequate representation of momentum transfer between the atmosphere and ocean within the WRF-SWAN coupling under such high wind speed conditions.
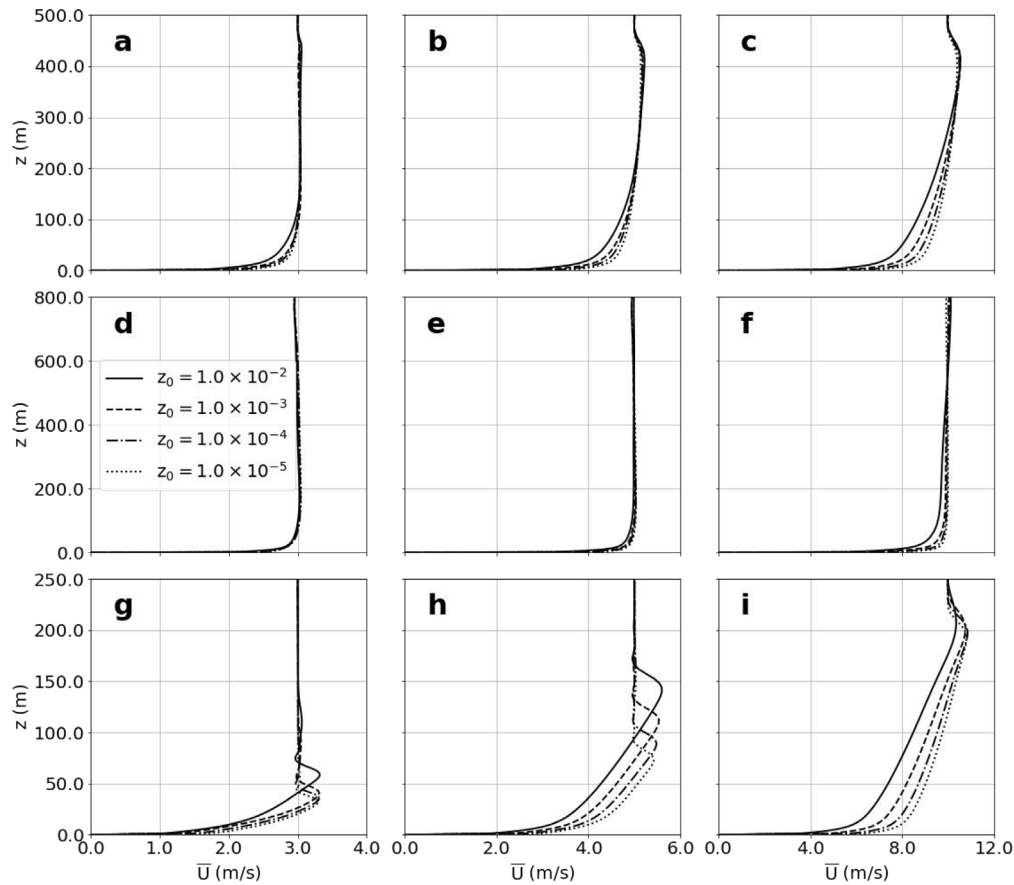
Fig. 4. Vertical profiles of horizontally-averaged wind speed. Columns 1, 2, and 3 represent $U_g = 3.0$, 5.0, and $10.0\,m/s$. Rows 1, 2, and 3 are neutral, convective, and stable stability conditions.

Table 3
Statistics of the logarithm of roughness length from the simulation and the observation at FINO1 site.

Run	JUL			SEP		
ID	SD	MB	RMSE	SD	MB	RMSE
OBS	1.68	–	–	0.61	–	–
CHA	0.39	0.24	1.65	0.19	−0.81	0.69
DRE	0.62	0.08	1.65	0.27	−0.71	0.73
TAY	0.48	1.06	1.67	0.25	0.06	0.73
POR	0.58	0.40	1.62	0.29	−0.42	0.74

The wind and wave parameters predicted at the meso-scale level are utilized in four distinct roughness parameterization methods. These methods generate 2D time-varying roughness length inputs for the micro-scale PALM model. Additionally, the roughness length was estimated by assuming the logarithmic wind profile, i.e.

$$\overline{u}_h(z) = \frac{u_*}{\kappa}\left[\log\left(\frac{z-d}{z_0}\right) - \Psi\left(\frac{z}{L}\right)\right] \qquad (7)$$

where d is the displacement height and is set to zero for offshore conditions, and Ψ is the stability correction (Van Wijk et al., 1990). It is worth mentioning that there are several methods for evaluating z_0 and results from different methods could have discrepancies up to one or two orders of magnitude, as pointed out by He et al. (2019). There are two feasible approaches given the available data in this study: analytical calculation using data from a single reference height; and fitting the logarithmic wind profile into the mean wind speed measured at multiple height levels. The first approach turned out to provide some values that seemed unphysically large or small, probably caused by uncertainties intrinsic to the measurements and the occurrences

of non-logarithmic wind profiles as observed by Kettle (2014). The latter method, which takes use of data across various altitude levels, appeared to alleviate these issues, enhancing robustness and yielding more reasonable values. Therefore we employed the second method and fitted Eq. (7) into the hourly-averaged wind speed data collected from the mast tower at multiple heights. Fig. 8 displays the time series of the horizontally averaged z_0 from the meso-scale model alongside the roughness length estimates derived from observational data. The metrics of comparison including Standard Deviation (SD), Mean Bias (MB), and Root Mean Square Error (RMSE) are summarized in Table 3. It is crucial to note that the values of metrics are calculated based on the logarithm of $z0$. This means they reflect the magnitude differences rather than the values of z_0 itself.

In JUL, Charnock, Drennan, and Porchetta parameterizations provided consistent roughness lengths with small differences for the first 16 h, when the wind was relatively strong and there was a wind-sea regime. All parameterizations tended to give larger z_0 than the estimates during this period. As the wind speed and surface friction reduced, the roughness lengths from Drennan's method decreased more rapidly compared with Charnock parameterization. Porchetta's equation yielded larger z_0 than Drennan's and demonstrated higher variations than the other methods during the occurrence of the wind–wave misalignment. The fitted values of z_0 exhibited pronounced fluctuations. Such variability arises under conditions of weak wind, old sea, and stable atmospheric stability, where the wave-induced stress plays a crucial role and the assumption of Eq. (7) might not hold. The Taylor-Yelland method has the same trend but with the largest value (larger by nearly one order of magnitude) in comparison with the other three formulas. For SEP case, all four methods produced stable z_0 values, reflecting the prevailing stable atmospheric and wave conditions. For the majority of this period, the outputs from Charnock's and Drennan's
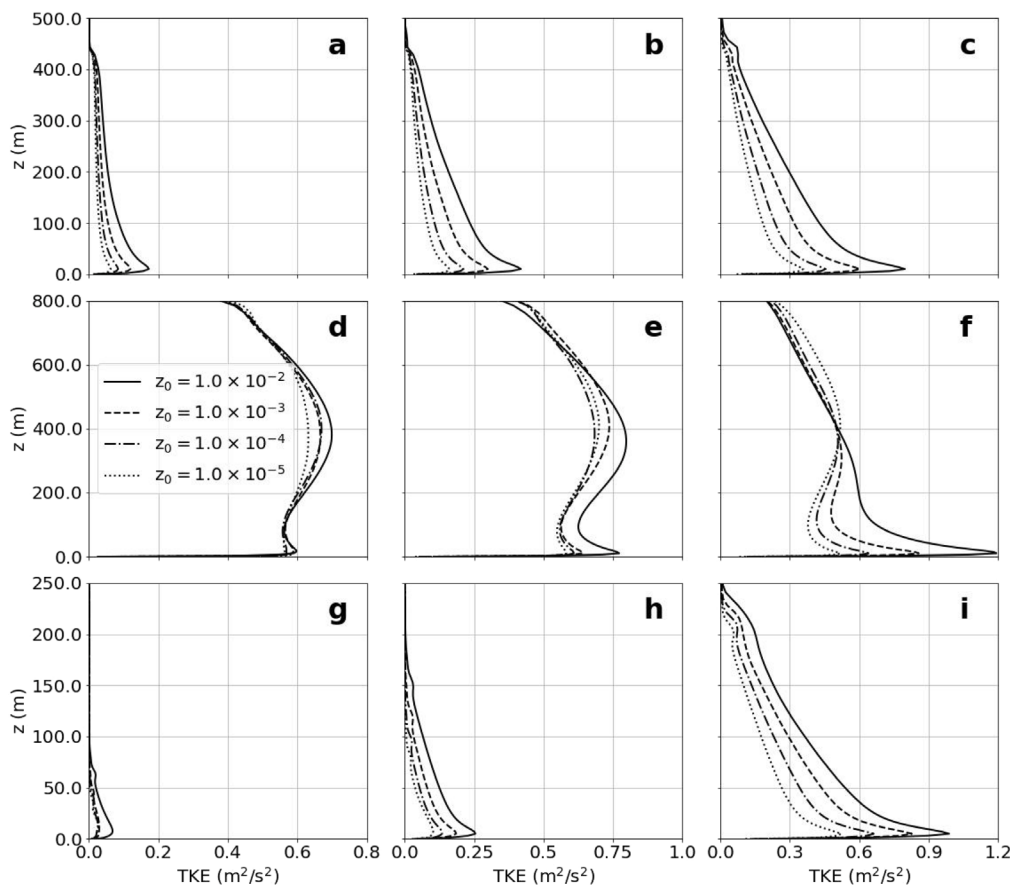
Fig. 5. Vertical profiles of turbulence kinetic energy. Columns 1, 2, and 3 represent U_g = 3.0, 5.0, and 10.0 m/s. Rows 1, 2, and 3 are neutral, convective, and stable stability conditions.
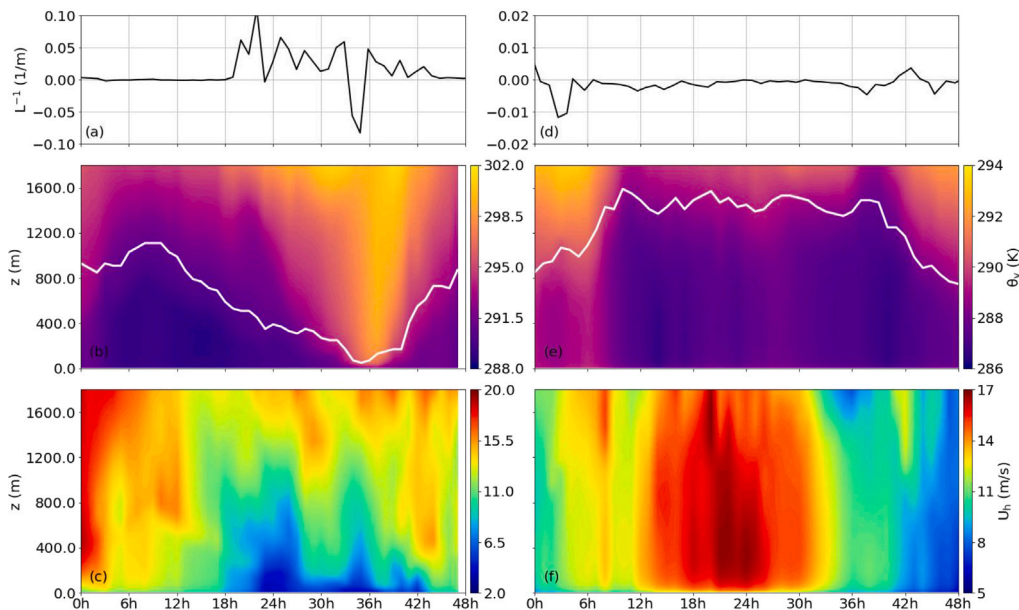

Fig. 6. (a,d) Time series of the reverse of the Monin–Obukhov length. (b,e) Time-height profiles of virtual potential temperature. (c,f) Time-height profiles of horizontal wind speed. The left column corresponds to JUL, while the right is for SEP. The white solid line represents the boundary layer height determined via the bulk Richardson number.

methods closely aligned. The Taylor-Yelland method again yielded the highest z_0, with Porchetta's parameterization sitting in between. The MB values presented in Table 3 imply that the results of Taylor-Yelland were the closest to the estimated values, closely followed by

the Porchetta method. In general, all parameterizations approximated the roughness length in consistency with the observation under wind-sea conditions, while failing to reproduce the estimated values under stable conditions with weak winds. Taylor-Yelland outstands the others
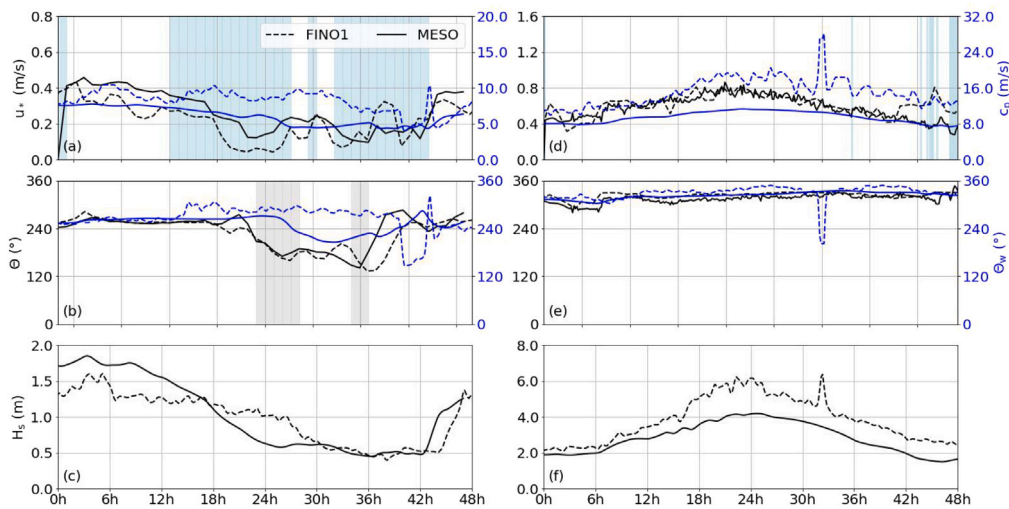
Fig. 7. (a,d) Time series of friction velocity (black) and wave phase speed (blue), with periods of old sea conditions shaded in light blue. (b,e) Time series of directions for wind (black) and wave (blue), with periods of wind–wave misalignment highlighted by a gray shade. (c,f) Time series of significant wave height. The left column corresponds to JUL, while the right is for SEP. The solid lines represent the results from the meso-scale model, and the dashed lines are the measurements from the FINO1 platform.
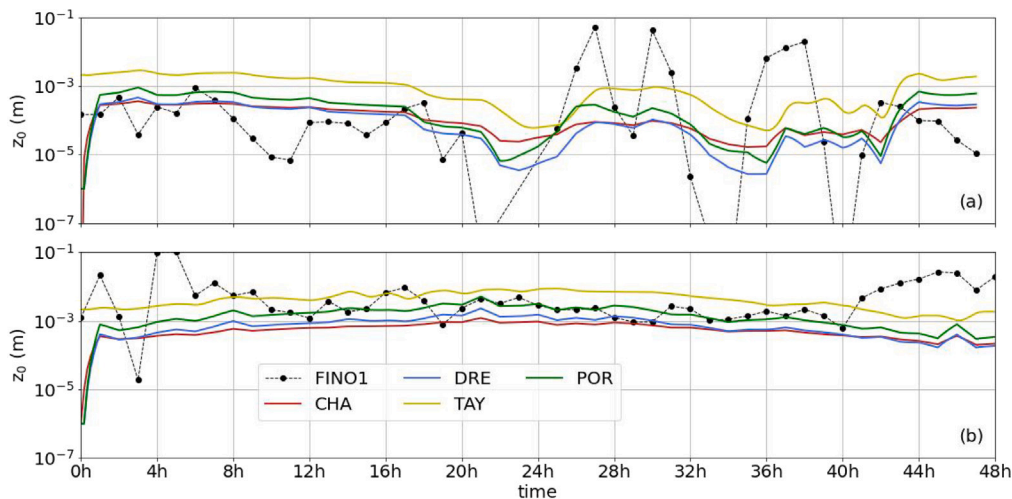

Fig. 8. Time series of the estimated roughness length based on measurement (dotted line with black circle) and the roughness lengths derived from four parameterizations (solid lines with colors) in JUL case (a) and SEP case (b).

under high wind speed and strong waves and tends to overestimate z_0 under modest wind periods.

4.2.2. Mean flow

The time series of mean wind speed and direction at the height of 40 m from the large-eddy simulations (using four roughness parameterizations) are compared with the WRF and the measurement data at FINO1 in Fig. 9. During the day of 06 in July, the meso-scale model captured well the shift of the wind direction and the decline in wind speed but overestimated the wind speed by approximately 2 m/s. Micro-scale simulations closely mirrored the WRF results during this time. Subsequently, from 00:00 to 12:00 on 07 July, PALM produced a more pronounced rebound of the wind speed than WRF during the transition from a neutral to a stable condition. All models predicted a turning of wind direction from south to west at 12:00 on 07 July, roughly 3 h ahead of the observation. In the case of September, the modeled wind directions by both WRF and PALM were aligned with the measurement. Notably, the WRF predicted wind speeds that were 3 m/s slower than observed over almost the two-day span. In contrast, the micro-scale model's predictions closely resembled the measurements. This suggests that enhancing resolution and capturing finer flow structures allows

the micro-scale model to refine local mean wind predictions under certain circumstances. The differences among simulations with the four parameterizations were trivial in both wind speed and direction.

Tables 4 and 5 present a comprehensive assessment of various models' efficacy in forecasting mean wind, detailing statistics such as Standard Deviation (SD), Mean Bias (MB), and Root Mean Square Error (RMSE) for the 1-hour averaged wind speed and direction from all models. For the July case, all models exhibited comparable performance. The Taylor-Yelland method yielded the smallest mean bias of 0.66 m/s and a standard deviation of 2.71 m/s, closely matched with observed data. LES models using alternative parameterizations did not show superiority to the WRF model, which produced the lowest RMSE of 1.95 m/s. Furthermore, WRF outperformed LES models in predicting wind direction with smaller values of MB and RMSE. However, compared to WRF, the micro-scale models exhibited notable improvement in the mean wind for the case in September, reducing the MB for wind speed and direction by approximately 3 m/s and 15° respectively. In general, the Taylor-Yelland method outperformed the other three roughness models, with smaller MB and RMSE in both cases. Nevertheless, the disparities between the four roughness parameterizations across all statistics are minor, with a magnitude of
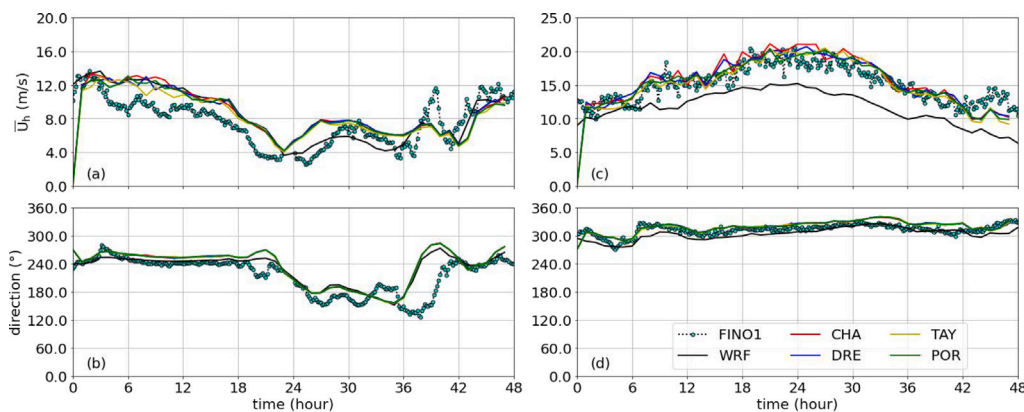
Fig. 9. Time series of (a,c) mean wind speed and (b,d) wind direction at the height of 40 m by WRF and multi-scale simulations with different roughness parameterization methods, compared with sonic data at FINO1. The left column corresponds to data for JUL while the right column shows data for SEP.

Table 4
Statistics of mean wind speed (m/s) from the simulation and the observation at FINO1 site.

Run	JUL			SEP		
ID	SD	MB	RMSE	SD	MB	RMSE
OBS	2.67	–	–	2.73	–	–
WRF	3.16	0.88	1.95	2.29	−3.27	3.61
CHA	2.95	1.01	2.64	4.05	0.49	2.57
DRE	2.78	0.96	2.58	3.83	0.31	2.40
TAY	2.71	0.66	2.47	3.95	−0.08	2.33
POR	2.78	0.88	2.56	3.78	0.12	2.30

Table 5
Statistics of mean wind direction (°) from the simulation and the observation at FINO1 site.

Run	JUL			SEP		
ID	SD	MB	RMSE	SD	MB	RMSE
OBS	37.7	–	–	10.3	–	–
WRF	32.3	13.2	30.1	12.5	−14.8	16.7
CHA	37.3	19.1	35.0	13.2	0.1	9.1
DRE	37.2	19.1	35.1	13.4	0.2	9.2
TAY	37.4	18.8	34.9	13.4	0.2	9.3
POR	37.3	19.1	35.1	13.3	0.4	9.1

0.1 m/s. This trend also persists at higher levels (data not presented here). This implies that modifying the roughness length based on the bulk wave parameters for micro-scale simulation is not an effective way to improve its performance in predicting the mean wind speed and direction.

Fig. 10 compares the simulated vertical profiles of 1-hour averaged wind speed and wind direction with lidar measurements at three different times. For the two times in July, the WRF model generated the vertical wind profiles in good agreement with the lidar data. The LES models roughly aligned with WRF at 15:10 on 06 July, with visible differences of less than 1 m/s among various roughness parameterizations under 400 m height. As the atmospheric condition shifted towards a stable state, the lower atmospheric layer exhibited declining wind speeds, leading to an enhanced gradient in wind speed and a marked wind veer near the ocean surface as shown in Fig. 10b and e. Distinctions in the mean wind became virtually negligible across all roughness length models under this scenario. At 12:30 on 06 September, the wind data collected from lidar depicted an almost uniform vertical wind distribution originating from the northeast. The PALM outputs aligned perfectly with the lidar data, while the wind speeds from the WRF model were lower than the observed values. This discrepancy could be attributed to WRF's parameterized representation of turbulence and its coarser grid resolution, which might not capture some of the finer-scale flow structures at specific local positions.

To further shed light on the sensitivity of wind shear and wind veer in micro-scale model to different roughness parameterizations, the LES with Charnock parameterization was used as a reference case, and its discrepancies in mean wind speed from the other three roughness length models at multiple heights were calculated for each hour in JUL and SEP and classified into three bins: slow wind ($\overline{u}_{h,10} < 5\,\mathrm{m/s}$), modest wind ($5\,\mathrm{m/s} < \overline{u}_{h,10} < 10\,\mathrm{m/s}$), strong wind ($\overline{u}_{h,10} > 10\,\mathrm{m/s}$). The vertical profiles of these results are plotted in Fig. 11 (different scales for x-axis), with the circles and the whiskers marking respectively the average and the standard deviation of the series of $\Delta\overline{u}_h$ at all time points for each bin. Fig. 11 shows that the Taylor-Yelland method gave the lowest mean wind speed in all bins. Results of Drennan's method were the closest to Charnock for modest and strong wind conditions, with its largest discrepancy reaching −0.5 m/s at the surface. Porchetta's method provided wind speeds slightly less than Drennan's due to the additional roughness from wind–wave misalignment. These results are highly correlated to the roughness length results in Fig. 8 because a larger roughness length means stronger surface drag and thus lower wind velocity. Furthermore, these discrepancies due to roughness are of a magnitude of roughly 10% of the absolute wind speed at the surface and rapidly tend to disappear as height increases, especially in low wind speed cases.

4.2.3. Turbulence

Turbulence in the boundary layer plays an important role in the exchange of mass, momentum, and energy between the atmosphere and the ocean. Due to the coarse mesh resolution (normally over a few hundred meters), the turbulent flows in the meso-scale model are highly parameterized and the direct resolving of turbulent structures is only possible in the micro-scale model. However, the simulation of turbulence in a meso-to-micro coupled modeling framework is a challenging task. Within a limited fetch region, the turbulence in LES cannot adapt itself to a fully developed state in equilibrium with the time-varying driving forces from the meso-scale model. A common solution is to accelerate the development of turbulence by applying temperature perturbation (Muñoz-Esparza et al., 2014; Muñoz-Esparza and Kosović, 2018) or synthetic turbulent velocity (Xie and Castro, 2008; Kim et al., 2013) (as in PALM) at boundaries of the outermost domain in the micro-scale model. Specifically, the unscaled turbulent motions are first determined by the time and length scales along three directions, and then multiplied by the amplitude tensor derived from Reynolds stresses to obtain the synthetic turbulence inflow. The turbulent time and length scales and the Reynolds stresses are not directly available, thus they are parameterized in PALM using the information of friction velocity, boundary layer height, Obukhov length, etc. at each time step (Kadasch et al., 2021). In this generation process, the roughness length is an essential quantity in MOST to determine the
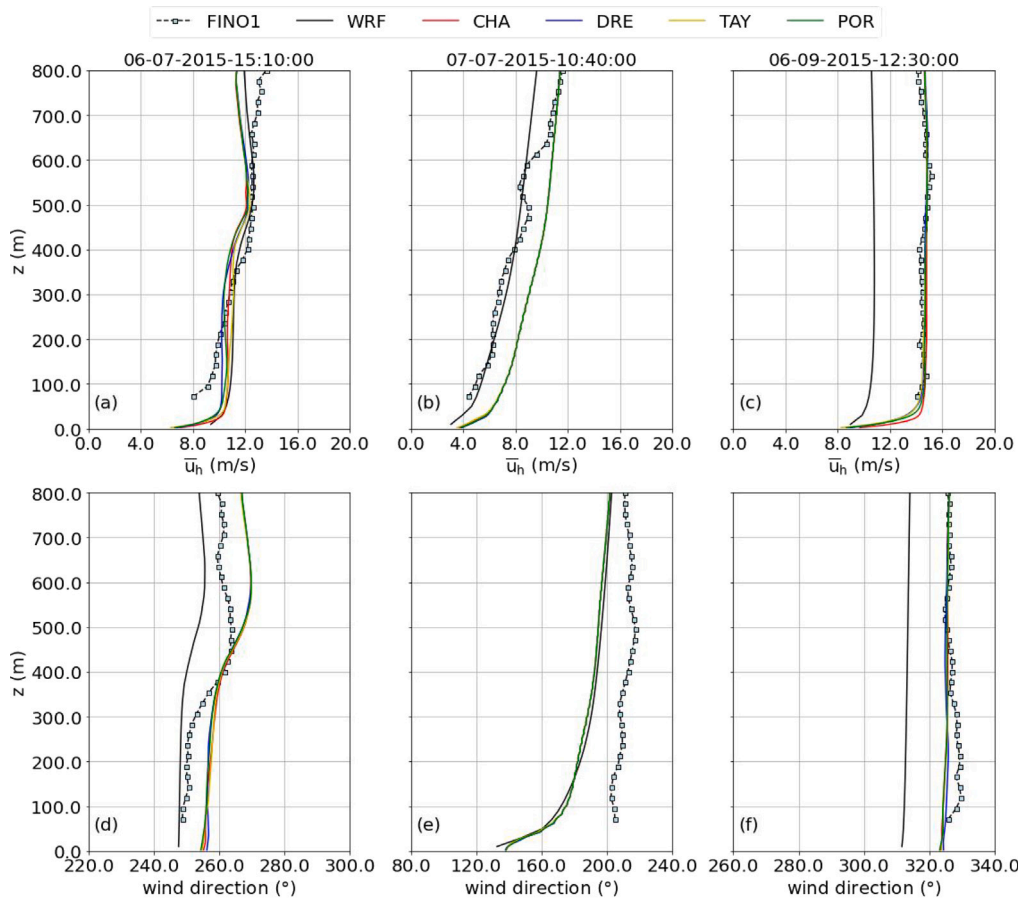
Fig. 10. Vertical profiles of 1-hour averaged (a,b,c) horizontal wind speed and (d,e,f) wind direction at 15:10 on July 6, 10:40 on July 7, and 12:30 on September 6. The dashed lines with square markers represent the lidar data.
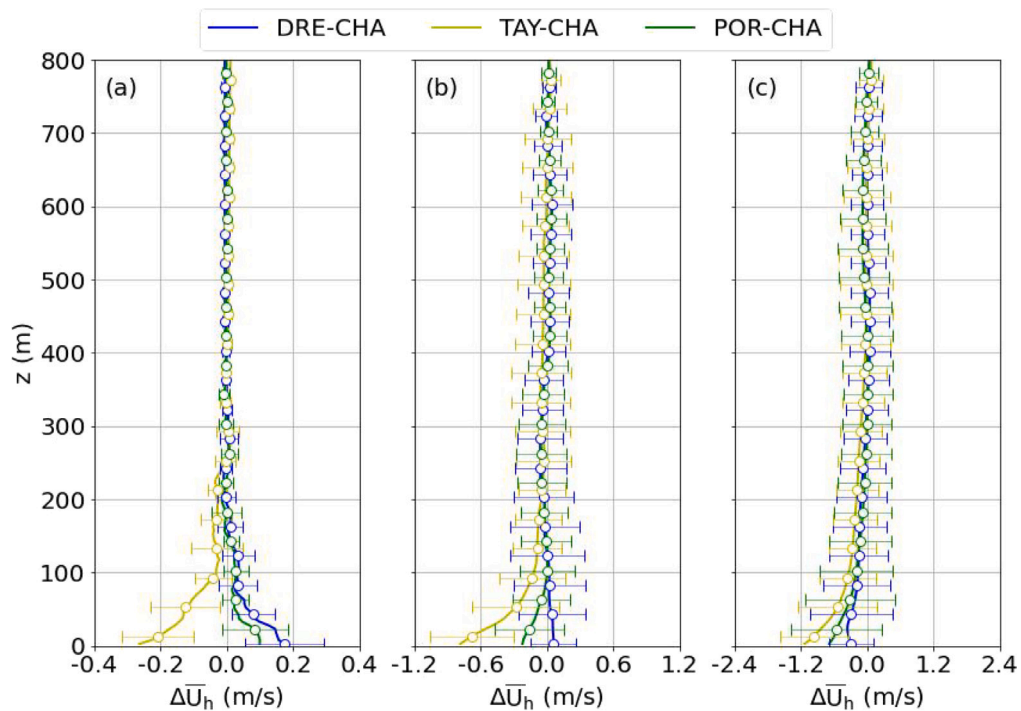

Fig. 11. Vertical profiles of the differences in mean wind speed among large-eddy simulations with the Charnock's and other three roughness parameterizations, classified into three wind speed bins: (a) low wind, (b) modest wind and (c) strong wind. The circle marker is the mean bias and the whisker marks the root mean square deviations.
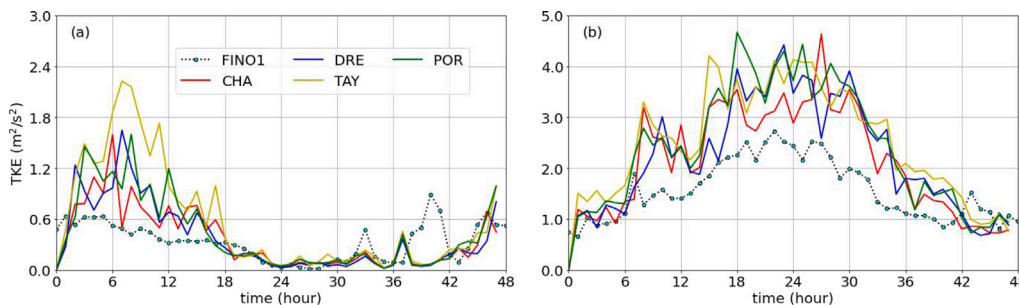
Fig. 12. Time series of turbulence kinetic energy at the height of 40 m by multi-scale simulations with different roughness parameterization methods, compared with sonic data at FINO1. (a) and (b) correspond to data for JUL and SEP respectively.

Table 6
Statistics of TKE (m^2/s^2) from the simulation and the observation at FINO1 site.

Run	JUL			SEP		
ID	SD	MB	RMSE	SD	MB	RMSE
OBS	0.22	–	–	0.59	–	–
CHA	0.35	0.04	0.31	1.18	0.44	0.91
DRE	0.39	0.05	0.35	1.07	0.45	0.80
TAY	0.62	0.25	0.61	1.11	0.78	1.07
POR	0.43	0.10	0.39	1.31	0.75	1.14

Obukhov length and the friction velocity and hence can affect the turbulent statistics in the micro-scale model.

Fig. 12 illustrates the time series of turbulence kinetic energy at height of 40 m from LES cases and the observational data. The micro-scale simulations effectively reproduced the evolution of the turbulence kinetic energy. This includes the suppressed low-level turbulence intensity due to thermal effects observed during the stable boundary layer on 07 July, as well as the oscillating trend noted in the SEP scenario. Nevertheless, it is also shown that PALM overestimated TKE for the periods under neutral conditions in both July and September. This is clearly shown in Table 6, which summarizes the metrics for the comparison in TKE between LES models and measurements. Especially for the SEP case, TKE values from LES models have a mean bias from $0.44\,m^2/s^2$ (CHA) to $0.78\,m^2/s^2$ (TAY). Since the mean wind profile was in very good agreement with the lidar data and the effects of atmospheric stability can be excluded (fully neutral condition), one source of the bias may come from the synthetic turbulence generator itself acting at the lateral boundaries of the LES domain. This indicates that the algorithm for estimating Reynolds stresses as mentioned above needs to be further calibrated.

Fig. 13 depicts the TKE profiles from four LES scenarios at three distinct time points, consistent with those in Fig. 10. These are compared against measurements taken at heights of 40 m, 60 m, and 80 m (only available for September). The upper row spans a vertical range up to 800 m, while the lower row provides a more detailed view, focusing on height below 120 m. Regardless of the roughness conditions, the TKE outcomes by LES exhibit similar vertical trends throughout the boundary layer, with a maximum peak close to the surface (about 20 m height) and continuously descending at higher levels. At 10:40 on 07 July, there was a notable decline in the simulated TKE beyond the boundary layer height, while this is not clearly reflected by the observed values. Such discrepancy can be traced back to the inherent inaccuracies in the meso-scale model during dynamic downscaling.

As the case in the analysis of mean wind, the simulation with Charnock's method was used as a reference, and the vertical profile of its differences ΔTKE compared with the other cases are classified into the low wind, modest wind, and strong wind bins and shown in Fig. 14 (different scales for x-axis). It shows the Taylor-Yelland case yielded the largest TKE, followed by the Porchetta method. Drennan's formula produced TKE very close to Charnock. The scale of the discrepancies among parameterizations highly depends on the strength of the wind and the height. For the low wind scenario, TKE results from all cases are almost identical, while they deviated from each other by a magnitude of $1.0\,m^2/s^2$ under strong wind conditions. Yet, the differences in terms of mean bias among all cases are very small and only visible under the height of 100 m. This illustrates that the TKE in meso-to-micro coupled scale simulation depends more on the driving forces from the meso-scale model rather than the roughness parameterization methods. Especially when the wind speed is lower than 5 m/s, the differences caused by roughness parameterizations are not distinguishable.

To evaluate the micro-scale model's capability in representing the energy cascade across the frequency domain, we sourced time series data of all three wind velocity components from the innermost domain (D06) of the large-eddy simulation. This data was sampled with a frequency of 20 Hz at a height of 40 m at the FINO1 site. The Power Spectral Density (PSD) curves at three time points (the same as in previous analysis) are computed using Welch's method and the resulting PSD curves are plotted in Fig. 15.

According to Kolmogorov's theory (Kolmogorov, 1941), the turbulent spectra can be divided into three ranges: the energy-containing range, where most of the turbulent kinetic energy is contained and influenced by the boundary and external forcing; the dissipative range, where the smallest turbulent eddies are dissipated and transformed into heat; the inertial subrange lying between, where the turbulence is locally isotropic and follows a cascade rate of $-5/3$ in a log–log plot that can be used to validate the quality of turbulence data. This $-5/3$ law can be seen in both measurements and LES results for the two neutral scenarios (15:10 on 06 July and 12:30 on 06 September) as shown in Fig. 15. The wind spectra from simulations start to deviate from the measurement at a frequency around 0.1 Hz and drop rapidly as frequency further increases due to the limit in mesh resolution (10 m in our case). One characteristic of the turbulence in the energy-containing range is that the eddies were constrained by the existence of the sea surface and thus showed a higher spectral density in the horizontal direction than in the vertical direction. This feature was also correctly captured by the micro-scale model. For the stable case at 10:40 on 07 July, the LES model showed a lower energy density than the observation and a lower drop-off frequency than in neutral cases. These discrepancies cannot be effectively reduced by any of the roughness parameterizations. Though the differences among various roughness length methods were distinguishable, no significant influences of the roughness length were found on neither the turbulent energy level nor distribution in the energy-containing range.
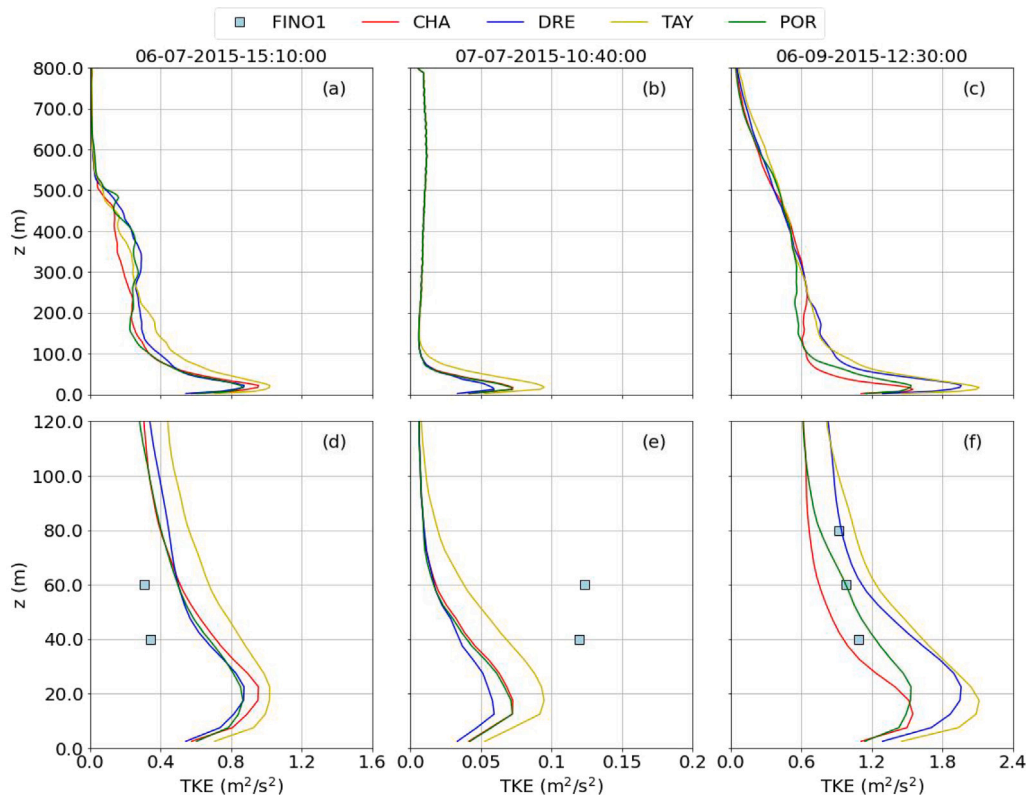
Fig. 13. Vertical profiles of turbulence kinetic energy at (a) 15:10 on July 6, (b) 10:40 on July 7, and (c) 12:30 on September 6. The second row (d,e,f) provides the zoom-in plots with the vertical extent to 120 m. The square markers represent the sonic data.
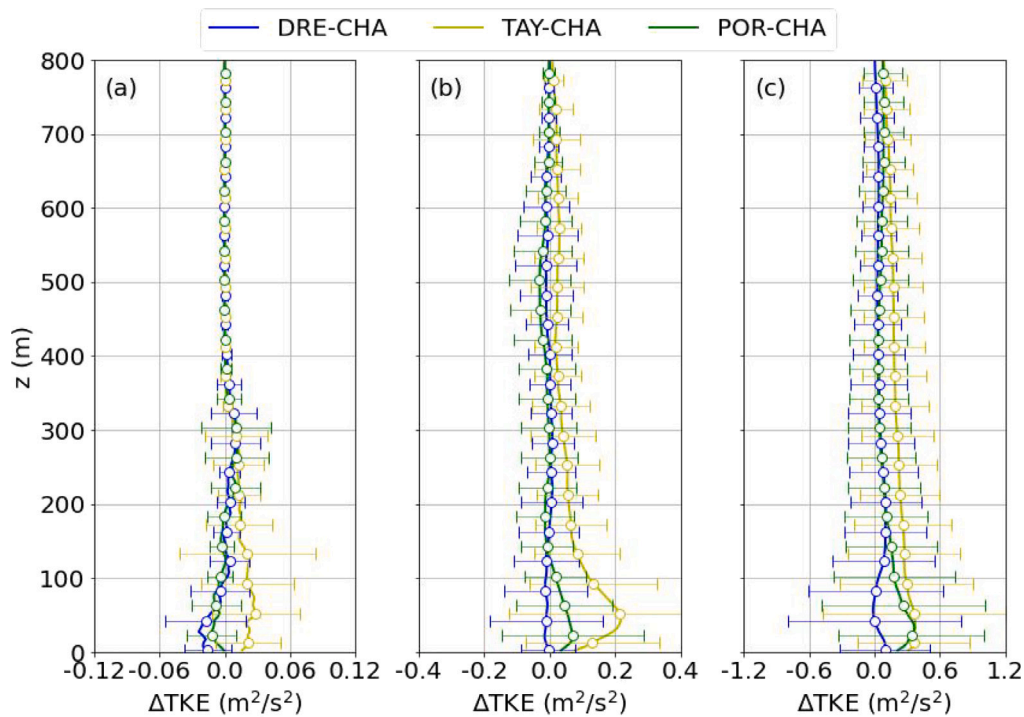

Fig. 14. Vertical profiles of the differences in turbulence kinetic energy among large-eddy simulations with the Charnock's and other three roughness parameterizations, classified into three wind speed bins: (a) low wind, (b) modest wind and (c) strong wind. The circle marker is the mean bias and the whisker marks the root mean square deviations.
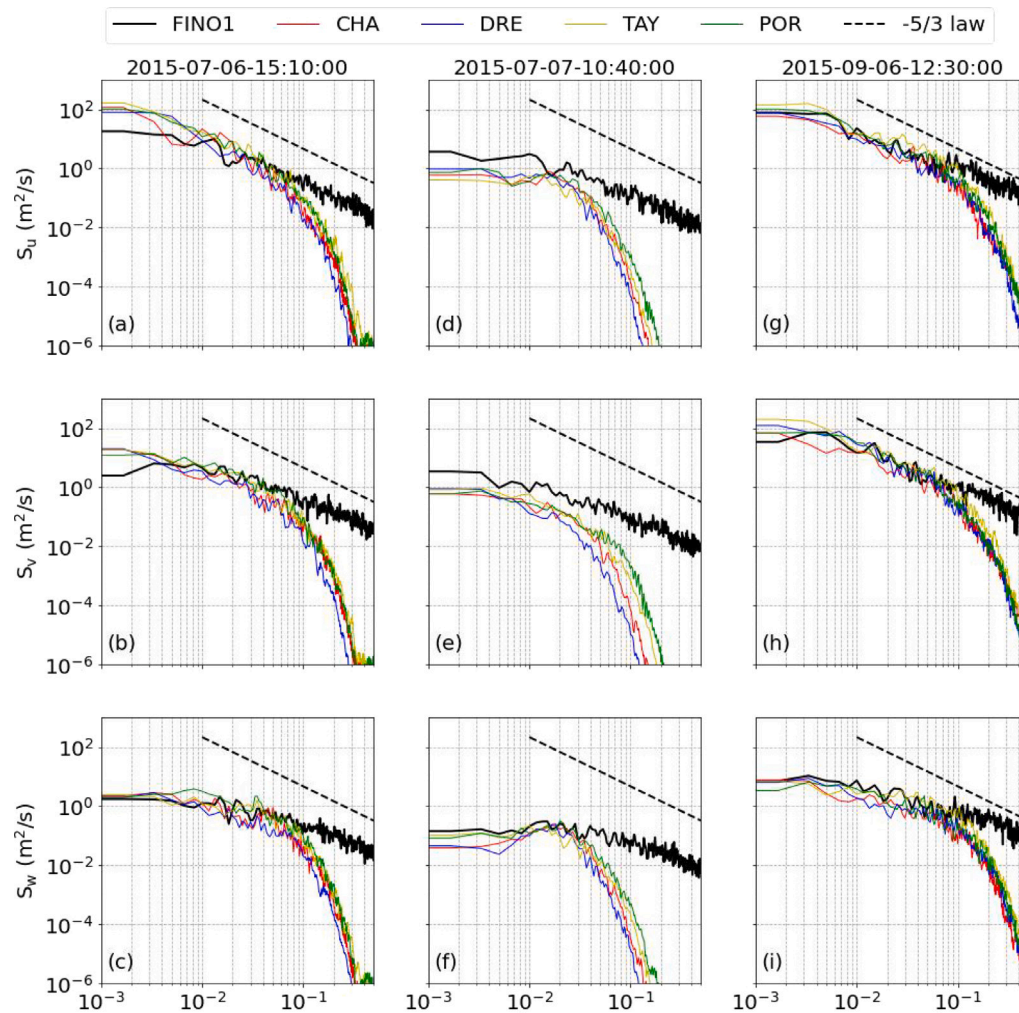
Fig. 15. PSD curves for (a, d, g) u, (b, e, h) v, and (c, f, i) w at 40 m height in four LES cases (color lines) are compared with the sonic data from FINO1 mast (black line). The dashed line represents the −5/3 slope for the inertial subrange.

5. Discussion and conclusion

In this research, we employ a novel multi-scale atmosphere–wave integrated modeling chain to simulate marine atmospheric boundary layer flows over the FINO1 region under realistic wind–wave regimes. The micro-scale model, PALM is driven by the meso-scale inputs from the WRF model and incorporates wave data from the SWAN model to generate a time-varying roughness length accounting for wave effects. The efficacy of this integrated modeling chain is evaluated by comparing simulated mean wind and turbulence results with actual measurements. We assess the performance of this model chain by comparing the mean wind and turbulence with the measurements and investigate the sensitivity of the micro-scale model to the widely used roughness parameterization methods.

We started our investigation with a set of idealized, stand-alone PALM simulations to provide fundamental insights into the effects of roughness length on boundary layer flows. Our findings highlighted that the impact of roughness lengths is tied to near-surface wind speeds and atmospheric stability conditions. Notably, the roughness length plays a pronounced role under stable conditions with strong wind speeds. However, its influence substantially wanes under convective scenarios or when wind velocities decrease, aligning with the findings of Lange et al. (2004). Based on this observation, we selected July 6–8 and September 5–7 in 2015 as two study periods for the meso-to-micro multiscale modeling. These scenarios offer a spectrum of atmospheric conditions, spanning from neutral to stable conditions, and encapsulate

both wind-sea and old sea regimes with various degrees of wind–wave misalignment.

Our simulations demonstrated a strong alignment with the observational data from the FINO1 platform, particularly in terms of mean wind speed and direction. The transition from a neutral to a stable boundary on 06 July, caused by warm air overriding the cooler ocean surface, was adeptly represented by the meso-scale model and then accurately downscaled to the PALM model. During September, both meso and micro-scale models effectively replicated the large-scale wind speed variations. Notably, the micro-scale model, which explicitly resolves finer flow structures, showed an enhanced predictive accuracy, aligning more closely with the observation. For the scenarios under consideration, the Charnock, Drennan, and Porchetta parameterizations yielded similar values for roughness length, which were almost an order of magnitude less than what the Taylor-Yelland method provided. Yet, despite these differences in parameterizations, there were no substantial variations in the mean wind speed and direction across all height levels. The deviations due to roughness are approximately 10% of the absolute wind speed at the surface, and these diminish rapidly with increased altitude, particularly in instances of low wind speed. Turbulence exhibits greater sensitivity to parameterization choices than mean wind. However, the differences remain minimal and are predominantly discernible within a height of 100 m. The trend of reduced roughness length influence as height increases was also observed by Türk and Emeis (2010) in their measurements from the FINO1 region. Additionally, during the specified periods, PALM

exhibited a tendency to over-predict the turbulence kinetic energy in the neutral boundary layer. This overestimation might stem from the synthetic turbulence generator integrated into the PALM framework, especially given that the mean wind speed was accurately predicted. Nevertheless, PALM offered a more enriching depiction of turbulence, effectively reproducing the energy cascade in the energy-containing range and inertial subrange right down to the finest resolved scale.

The present work establishes a modeling chain capable of representing the multi-scale boundary layer flows in realistic wind–wave conditions. Such a framework offers the chance to advance further studies of offshore meteorology and wind energy applications. Based on findings from both idealized and realistic multi-scale simulations, we conclude that the micro-scale model shows minimal sensitivity to the choice of roughness length parameterization in the meso-to-micro modeling process, in terms of both mean wind and turbulence characteristics. This indicates that alternating roughness parameterization methods cannot achieve a significant improvement in the prediction by this type of modeling. It should be noted that this conclusion is based on the currently used modeling framework and is limited by the coupling technique between meso and micro-scale models. Exploring the efficacy of roughness parameterizations in alternative meso-to-micro scale coupling tactics, such as two-way coupling or internal forcing over boundary condition-driven approaches (Allaerts et al., 2020) merits further investigation. Developing more advanced wind–wave coupling methods that can better represent the wind–wave interaction process should also be the focus of future studies.

CRediT authorship contribution statement

Xu Ning: Methodology, Investigation, Software, Writing – original draft, Formal analysis, Validation, Writing – review & editing. **Mostafa Bakhoday Paskyabi:** Supervision, Conceptualization, Software, Data curation, Funding acquisition, Writing – review & editing. **Hoang Hai Bui:** Software, Writing – review. **Mohammadreza Mohammadpour Penchah:** Software, Writing – review.

Declaration of competing interest

The authors declare that they have no known competing financial interests or personal relationships that could have appeared to influence the work reported in this paper.

Data availability

Data will be made available on request.

Acknowledgments

References

Allaerts, D., Quon, E., Draxl, C., Churchfield, M., 2020. Development of a time–height profile assimilation technique for large-eddy simulation. Bound.-Lay. Meteorol. 176 (3), 329–348.

AlSam, A., Szasz, R., Revstedt, J., 2015. The influence of sea waves on offshore wind turbine aerodynamics. J. Energy Resour. Technol. 137 (5).

Arthur, R.S., Mirocha, J.D., Marjanovic, N., Hirth, B.D., Schroeder, J.L., Wharton, S., Chow, F.K., 2020. Multi-scale simulation of wind farm performance during a frontal passage. Atmosphere 11 (3), 245.

Bakhoday-Paskyabi, M., Bui, H., Mohammadpour-Penchah, M., 2022a. Atmospheric-wave multi-scale flow modelling. HIPERWIND EU project, delivery 2.1.

Bakhoday-Paskyabi, M., Krutova, M., Bui, H., Ning, X., 2022b. Multiscale simulation of offshore wind variability during frontal passage: Brief implication on turbines' wakes and load. In: Journal of Physics: Conference Series. IOP Publishing, 012003.

Booij, N., Holthuijsen, L., Ris, R., 1997. The" SWAN" wave model for shallow water. In: Coastal Engineering 1996. pp. 668–676.

Bui, H., Bakhoday-Paskyabi, M., 2022. Mesoscale simulation of open cellular convection: Roles of model resolutions and physics parameterizations. In: Journal of Physics: Conference Series. IOP Publishing, 012006.

Charnock, H., 1955. Wind stress on a water surface. Q. J. R. Meteorol. Soc. 81 (350), 639–640.

Cohen, J., Belcher, S., 1999. Turbulent shear flow over fast-moving waves. J. Fluid Mech. 386, 345–371.

Deardorff, J.W., 1980. Stratocumulus-capped mixed layers derived from a three-dimensional model. Bound.-Layer Meteorol. 18 (4), 495–527.

Deskos, G., Lee, J.C., Draxl, C., Sprague, M.A., 2021. Review of wind–wave coupling models for large-eddy simulation of the marine atmospheric boundary layer. J. Atmos. Sci. 78 (10), 3025–3045.

Donelan, M.A., 1982. The dependence of the aerodynamic drag coefficient on wave parameters. In: Proc. First Int. Conf. on Meteorol. and Air-Sea Interaction of the Coastal Zone. Amer. Meteor. Soc., pp. 381–387.

Draxl, C., Allaerts, D., Quon, E., Churchfield, M., 2021. Coupling mesoscale budget components to large-eddy simulations for wind-energy applications. Bound.-Lay. Meteorol. 179 (1), 73–98.

Drennan, W.M., Graber, H.C., Hauser, D., Quentin, C., 2003. On the wave age dependence of wind stress over pure wind seas. J. Geophys. Res.: Oceans 108 (C3).

Drennan, W.M., Taylor, P.K., Yelland, M.J., 2005. Parameterizing the sea surface roughness. J. Phys. Oceanogr. 35 (5), 835–848.

Dudhia, J., 1989. Numerical study of convection observed during the winter monsoon experiment using a mesoscale two-dimensional model. J. Atmos. Sci. 46 (20), 3077–3107.

Grooms, I., Julien, K., 2018. Multiscale models in geophysical fluid dynamics. Earth Space Sci. 5 (11), 668–675.

Han, Y., Shen, L., Xu, G., Cai, C., Hu, P., Zhang, J., 2018. Multiscale simulation of wind field on a long-span bridge site in mountainous area. J. Wind Eng. Ind. Aerodyn. 177, 260–274.

Hao, X., Shen, L., 2019. Wind–wave coupling study using LES of wind and phase-resolved simulation of nonlinear waves. J. Fluid Mech. 874, 391–425.

Haupt, S.E., Kosovic, B., Shaw, W., Berg, L.K., Churchfield, M., Cline, J., Draxl, C., Ennis, B., Koo, E., Kotamarthi, R., et al., 2019. On bridging a modeling scale gap: Mesoscale to microscale coupling for wind energy. Bull. Am. Meteorol. Soc. 100 (12), 2533–2550.

He, Y., Fu, J., Shu, Z., Chan, P., Wu, J., Li, Q., 2019. A comparison of micrometeorological methods for marine roughness estimation at a coastal area. J. Wind Eng. Ind. Aerodyn. 195, 104010.

Heinze, R., Moseley, C., Böske, L.N., Muppa, S.K., Maurer, V., Raasch, S., Stevens, B., 2017. Evaluation of large-eddy simulations forced with mesoscale model output for a multi-week period during a measurement campaign. Atmos. Chem. Phys. 17 (11), 7083–7109.

Hersbach, H., Bell, B., Berrisford, P., Hirahara, S., Horányi, A., Muñoz-Sabater, J., Nicolas, J., Peubey, C., Radu, R., Schepers, D., et al., 2020. The ERA5 global reanalysis. Q. J. R. Meteorol. Soc. 146 (730), 1999–2049.

Hong, S.-Y., Noh, Y., Dudhia, J., 2006. A new vertical diffusion package with an explicit treatment of entrainment processes. Mon. Weather Rev. 134 (9), 2318–2341.

Hsu, S.-A., 1974. A dynamic roughness equation and its application to wind stress determination at the air-sea interface. J. Phys. Oceanogr. 4 (1), 116–120.

Janssen, P.A., 1991. Quasi-linear theory of wind-wave generation applied to wave forecasting. J. Phys. Oceanogr. 21 (11), 1631–1642.

Jia, W., Zhang, X., 2020. The role of the planetary boundary layer parameterization schemes on the meteorological and aerosol pollution simulations: A review. Atmos. Res. 239, 104890.

Jiménez, P.A., Dudhia, J., González-Rouco, J.F., Navarro, J., Montávez, J.P., García-Bustamante, E., 2012. A revised scheme for the WRF surface layer formulation. Mon. Weather Rev. 140 (3), 898–918.

Kadasch, E., Sühring, M., Gronemeier, T., Raasch, S., 2021. Mesoscale nesting interface of the PALM model system 6.0. Geosci. Model Dev. 14 (9), 5435–5465.

Kalvig, S., Manger, E., Hjertager, B.H., Jakobsen, J.B., 2014. Wave influenced wind and the effect on offshore wind turbine performance. Energy Procedia 53, 202–213.

Kettle, A.J., 2014. Unexpected vertical wind speed profiles in the boundary layer over the southern North Sea. J. Wind Eng. Ind. Aerodyn. 134, 149–162.

Kim, Y., Castro, I.P., Xie, Z.-T., 2013. Divergence-free turbulence inflow conditions for large-eddy simulations with incompressible flow solvers. Comput. & Fluids 84, 56–68.

Kolmogorov, A.N., 1941. The local structure of turbulence in incompressible viscous fluid for very large Reynolds numbers. C. R. Acad. Sci. URSS 30, 301–305.

Lange, B., Larsen, S., Højstrup, J., Barthelmie, R., 2004. Importance of thermal effects and sea surface roughness for offshore wind resource assessment. J. Wind Eng. Ind. Aerodyn. 92 (11), 959–988.

Liu, C., Li, X., Song, J., Zou, Z., Huang, J., Zhang, J.A., Jie, G., Wang, J., 2022. Characteristics of the marine atmospheric boundary layer under the influence of ocean surface waves. J. Phys. Oceanogr. 52 (6), 1261–1276.

Liu, Y., Warner, T., Liu, Y., Vincent, C., Wu, W., Mahoney, B., Swerdlin, S., Parks, K., Boehnert, J., 2011. Simultaneous nested modeling from the synoptic scale to the LES scale for wind energy applications. J. Wind Eng. Ind. Aerodyn. 99 (4), 308–319.

Maronga, B., Banzhaf, S., Burmeister, C., Esch, T., Forkel, R., Fröhlich, D., Fuka, V., Gehrke, K.F., Geletič, J., Giersch, S., et al., 2020. Overview of the PALM model system 6.0. Geosci. Model Dev. 13 (3), 1335–1372.

Mazzaro, L.J., Muñoz-Esparza, D., Lundquist, J.K., Linn, R.R., 2017. Nested mesoscale-to-LES modeling of the atmospheric boundary layer in the presence of under-resolved convective structures. J. Adv. Modelling Earth Syst. 9 (4), 1795–1810.

Mirocha, J., Kosović, B., Kirkil, G., 2014. Resolved turbulence characteristics in large-eddy simulations nested within mesoscale simulations using the Weather Research and Forecasting Model. Mon. Weather Rev. 142 (2), 806–831.

Mlawer, E.J., Taubman, S.J., Brown, P.D., Iacono, M.J., Clough, S.A., 1997. Radiative transfer for inhomogeneous atmospheres: RRTM, a validated correlated-k model for the longwave. J. Geophys. Res.: Atmos. 102 (D14), 16663–16682.

Monin, A., 1954. Basic turbulent mixing laws in the atmospheric surface layer. Tr. Akad. Nauk SSSR Geofiz. Inst. 24, 163–187.

Morrison, H., Thompson, G., Tatarskii, V., 2009. Impact of cloud microphysics on the development of trailing stratiform precipitation in a simulated squall line: Comparison of one-and two-moment schemes. Mon. Weather Rev. 137 (3), 991–1007.

Mukul Tewari, N., Tewari, M., Chen, F., Wang, W., Dudhia, J., LeMone, M., Mitchell, K., Ek, M., Gayno, G., Wegiel, J., et al., 2004. Implementation and verification of the unified NOAH land surface model in the WRF model (Formerly Paper Number 17.5). In: Proceedings of the 20th Conference on Weather Analysis and Forecasting/16th Conference on Numerical Weather Prediction, Seattle, WA, USA, Vol. 14.

Munoz Esparza, D., 2013. Multiscale modelling of atmospheric flows: Towards improving the representation of boundary layer physics.

Muñoz-Esparza, D., Kosović, B., 2018. Generation of inflow turbulence in large-eddy simulations of nonneutral atmospheric boundary layers with the cell perturbation method. Mon. Weather Rev. 146 (6), 1889–1909.

Muñoz-Esparza, D., Kosović, B., Mirocha, J., van Beeck, J., 2014. Bridging the transition from mesoscale to microscale turbulence in numerical weather prediction models. Bound.-Layer Meteorol. 153 (3), 409–440.

Muñoz-Esparza, D., Lundquist, J.K., Sauer, J.A., Kosović, B., Linn, R.R., 2017. Coupled mesoscale-LES modeling of a diurnal cycle during the CWEX-13 field campaign: From weather to boundary-layer eddies. J. Adv. Modelling Earth Syst. 9 (3), 1572–1594.

Piroozmand, P., Mussetti, G., Allegrini, J., Mohammadi, M.H., Akrami, E., Carmeliet, J., 2020. Coupled CFD framework with mesoscale urban climate model: Application to microscale urban flows with weak synoptic forcing. J. Wind Eng. Ind. Aerodyn. 197, 104059.

Porchetta, S., Temel, O., Muñoz-Esparza, D., Reuder, J., Monbaliu, J., Van Beeck, J., van Lipzig, N., 2019. A new roughness length parameterization accounting for wind–wave (mis) alignment. Atmos. Chem. Phys. 19 (10), 6681–6700.

Prósper, M.A., Otero-Casal, C., Fernández, F.C., Miguez-Macho, G., 2019. Wind power forecasting for a real onshore wind farm on complex terrain using WRF high resolution simulations. Renew. Energy 135, 674–686.

Rai, R.K., Berg, L.K., Kosović, B., Haupt, S.E., Mirocha, J.D., Ennis, B.L., Draxl, C., 2019. Evaluation of the impact of horizontal grid spacing in terra incognita on coupled mesoscale–microscale simulations using the WRF framework. Mon. Weather Rev. 147 (3), 1007–1027.

Santoni, C., García-Cartagena, E.J., Ciri, U., Zhan, L., Valerio Iungo, G., Leonardi, S., 2020. One-way mesoscale-microscale coupling for simulating a wind farm in North Texas: Assessment against SCADA and LiDAR data. Wind Energy 23 (3), 691–710.

Sanz Rodrigo, J., Chávez Arroyo, R.A., Moriarty, P., Churchfield, M., Kosović, B., Réthoré, P.-E., Hansen, K.S., Hahmann, A., Mirocha, J.D., Rife, D., 2017. Mesoscale to microscale wind farm flow modeling and evaluation. Wiley Interdiscip. Rev.: Energy Environ. 6 (2), e214.

Skamarock, W.C., Klemp, J.B., Dudhia, J., Gill, D.O., Liu, Z., Berner, J., Wang, W., Powers, J.G., Duda, M.G., Barker, D.M., et al., 2019. A Description of the Advanced Research WRF Model Version 4, Vol. 145. National Center for Atmospheric Research, Boulder, CO, USA, p. 145.

Sullivan, P.P., McWilliams, J.C., 2010. Dynamics of winds and currents coupled to surface waves. Annu. Rev. Fluid Mech. 42, 19–42.

Sullivan, P.P., McWilliams, J.C., Patton, E.G., 2014. Large-eddy simulation of marine atmospheric boundary layers above a spectrum of moving waves. J. Atmos. Sci. 71 (11), 4001–4027.

Taylor, P.K., Yelland, M.J., 2001. The dependence of sea surface roughness on the height and steepness of the waves. J. Phys. Oceanogr. 31 (2), 572–590.

Temel, O., Bricteux, L., van Beeck, J., 2018. Coupled WRF-OpenFOAM study of wind flow over complex terrain. J. Wind Eng. Ind. Aerodyn. 174, 152–169.

Türk, M., Emeis, S., 2010. The dependence of offshore turbulence intensity on wind speed. J. Wind Eng. Ind. Aerodyn. 98 (8–9), 466–471.

Van Wijk, A., Beljaars, A., Holtslag, A., Turkenburg, W., 1990. Evaluation of stability corrections in wind speed profiles over the North Sea. J. Wind Eng. Ind. Aerodyn. 33 (3), 551–566.

Vollmer, L., Steinfeld, G., Heinemann, D., Kühn, M., 2016. Estimating the wake deflection downstream of a wind turbine in different atmospheric stabilities: an LES study. Wind Energy Sci. 1 (2), 129–141.

Wu, X., 2017. Inflow turbulence generation methods. Annu. Rev. Fluid Mech. 49, 23–49.

Wu, L., Rutgersson, A., Sahlée, E., Guo Larsén, X., 2016. Swell impact on wind stress and atmospheric mixing in a regional coupled atmosphere-wave model. J. Geophys. Res.: Oceans 121 (7), 4633–4648.

Xie, Z.-T., Castro, I.P., 2008. Efficient generation of inflow conditions for large eddy simulation of street-scale flows. Flow Turbul. Combust. 81 (3), 449–470.

Yang, D., Meneveau, C., Shen, L., 2014. Effect of downwind swells on offshore wind energy harvesting–a large-eddy simulation study. Renew. Energy 70, 11–23.

Zajaczkowski, F.J., Haupt, S.E., Schmehl, K.J., 2011. A preliminary study of assimilating numerical weather prediction data into computational fluid dynamics models for wind prediction. J. Wind Eng. Ind. Aerodyn. 99 (4), 320–329.

Zhang, C., Wang, Y., Hamilton, K., 2011. Improved representation of boundary layer clouds over the southeast Pacific in ARW-WRF using a modified Tiedtke cumulus parameterization scheme. Mon. Weather Rev. 139 (11), 3489–3513.